Article

Sorption Profile of Low Specific Activity ^{99}Mo on Nanoceria-Based Sorbents for the Development of ^{99m}Tc Generators: Kinetics, Equilibrium, and Thermodynamic Studies

Mohamed F. Nawar ^{1,2,*}, Alaa F. El-Daoushy ^{2}, Metwally Madkour ^{3} and Andreas Türler ^{1}

1 Department of Chemistry, Biochemistry and Pharmaceutical Sciences, Faculty of Science, University of Bern, Freiestrasse 3, CH-3012 Bern, Switzerland; andreas.tuerler@unibe.ch
2 Radioactive Isotopes and Generators Department, Hot Laboratories Center, Egyptian Atomic Energy Authority, Cairo 13759, Egypt; alaafeldaoushy@yahoo.com
3 Chemistry Department, Faculty of Science, Kuwait University, Safat 13060, Kuwait; metwally.madkour@ku.edu.kw
* Correspondence: mohamed.nawar@unibe.ch

Abstract: ^{99}Mo/^{99m}Tc generators play a significant role in supplying ^{99m}Tc for diagnostic interventions in nuclear medicine. However, the applicability of using low specific activity (LSA) ^{99}Mo asks for sorbents with high sorption capacity. Herein, this study aims to evaluate the sorption behavior of LSA ^{99}Mo towards several CeO$_2$ nano-sorbents developed in our laboratory. These nanomaterials were prepared by wet chemical precipitation (CP) and hydrothermal (HT) approaches. Then, they were characterized using XRD, BET, FE-SEM, and zeta potential measurements. Additionally, we evaluated the sorption profile of carrier-added (CA) ^{99}Mo onto each material under different experimental parameters. These parameters include pH, initial concentration of molybdate solution, contact time, and temperature. Furthermore, the maximum sorption capacities were evaluated. The results reveal that out of the synthesized CeO$_2$ nanoparticles (NPs) materials, the sorption capacity of HT-1 and CP-2 reach 192 ± 10 and 184 ± 12 mg Mo·g^{-1}, respectively. For both materials, the sorption kinetics and isotherm data agree with the Elovich and Freundlich models, respectively. Moreover, the diffusion study demonstrates that the sorption processes can be described by pore diffusion (for HT-synthesis route 1) and film diffusion (for CP-synthesis route 2). Furthermore, the thermodynamic parameters indicate that the Mo sorption onto both materials is a spontaneous and endothermic process. Consequently, it appears that HT-1 and CP-2 have favorable sorption profiles and high sorption capacities for CA-^{99}Mo. Therefore, they are potential candidates for producing a ^{99}Mo/^{99m}Tc radionuclide generator by using LSA ^{99}Mo.

Keywords: LSA ^{99}Mo; CeO$_2$ NPs; thermodynamic parameters; sorption kinetics; hydrothermal modification

1. Introduction

There is an increasing interest in using ^{99m}Tc (T$_{1/2}$ = 6.01 h) for diagnostic purposes in nuclear medicine and radiotracing applications in the industry [1–4]. This increased interest has heightened the need to produce ^{99}Mo/^{99m}Tc generators on a large scale. The production of these generators includes different technologies, for instance, sublimation, electrochemical, solvent extraction, supported liquid membrane (SLM), and column chromatographic approaches [5–9]. Among these generators, the portable column chromatographic type is considered the primary source to supply ready-to-use ^{99m}Tc onsite [7,10]. The idea of these generators is to retain the parent ^{99}Mo on a sorbent for decay so that the daughter ^{99m}Tc can then be easily separated in high purity by using an isotonic saline solution at desired time intervals [11,12].

The ^{99m}Tc parent, [99]Mo, can be produced in nuclear reactors either by fission of [235]U or by direct neutron irradiation of natural Mo or enriched [98]Mo targets [10,13]. On the one hand, fission produces more than 95% of the ^{99m}Tc generators on the market because it provides [99]Mo with high specific activity (>10^4 Ci/g Mo). On the other hand, this route has some disadvantages. The main ones are the prohibitive production costs, the generation of large amounts of radioactive waste, and the increasing proliferation risks [14–16]. To overcome these difficulties, many methods have been suggested for using neutron-activated [99]Mo of low specific activity (LSA) (~5–10 Ci/g Mo) [15,17–20]. However, the low sorption capacity of commercial materials is the most critical limitation, which reduces their applicability. It is worth mentioning that the retention capacity of alumina (Al_2O_3), the material used, is limited to only 2–20 mg.g^{-1} for molybdate ([99]MoO_4^{2-}) [8].

Recently, nanotechnology has shown that it has the potential to develop the properties of different materials. These newly developed materials provide attractive solutions in multidisciplinary sectors, such as biology, chemistry, and medical sciences [21]. Nanostructured materials possess a unique surface morphology, which derives from their small particle size structure, high surface area, and the large number of active sites. The successful synthesis of such nanostructured sorbents has been reported by using several approaches. Out of these techniques, wet-chemical precipitation and hydrothermal methods bring potential advantages. Wet chemical precipitation is a simple, cost-effective method that can be conducted at ambient temperature [22–24]. The hydrothermal route offers high product purity with uniform composition, less particle agglomeration, controlled surface morphology, and narrow particle size distribution [25,26]. Consequently, this unique surface morphology significantly improves sorption efficiency and high adsorbate selectivity [27]. In this context, the use of nanomaterial-based sorbents appears to be a promising solution to overcome the low sorption capacity of conventional sorbents for LSA [99]Mo. These new sorbents might make it possible to produce [99]Mo/^{99m}Tc generators by using LSA [99]Mo.

In this paper, our main objective is to evaluate the sorption profile of LSA [99]Mo on several CeO_2 nanosorbents developed in our laboratory. To achieve this goal, we report the preparation of CeO_2 NPs using wet chemical precipitation and hydrothermal methods. Moreover, we investigated the sorption efficiency of the prepared materials for Mo under different experimental conditions such as pH, the initial concentration of the molybdate solution, contact time, and temperature. In addition, the sorption kinetics, equilibrium isotherm, and thermodynamics were evaluated.

2. Materials and Methods

2.1. Materials

All chemicals were of analytical grade purity and were used without further purification. Milli-Q water was used for the preparation of solutions and washings. Cerium nitrate hexahydrate $Ce(NO_3)_3 \cdot 6H_2O$, sodium hydroxide, ethanol absolute, and nitric acid were purchased from Merck, Darmstadt, Germany.

[99]Mo radiotracer solution was obtained by eluting 57.1 GBq fission [99]Mo alumina-based [99]Mo/^{99m}Tc generator (Pertector, National Centre for Nuclear Research, Otwock, Poland) with 5 mL 1 M NaOH solution after ~7 d from the calibration date. The total [99]Mo radioactivity was measured with a Capintec Radioisotopes Calibrator (model CRC-55tR Mirion Technologies, Inc., Florham Park, NJ, USA). The [99]Mo eluate solution was passed through 0.45 micro-Millipore filter to retain any alumina particles. Then, the [99]Mo solution was diluted with HNO_3 solution to the desired pH value.

2.2. Instrumentation

Radiometric identifications and measurements were carried out by using a multichannel analyzer (MCA), Inspector 2000 model, Canberra Series, Mirion Technologies, Inc., Meriden, CT, USA, coupled with a high-purity germanium detector (HPGe). Samples of constant geometry were counted at a low dead time (<5%). The radioactivity levels were determined by quantifying the 740 keV photo peaks corresponding to [99]Mo. A pH-meter

with a microprocessor (Mettler Toledo, Seven Compact S210 model, Greifensee, Switzerland) was used to measure the pH values. A thermostated shaking water bath (Julabo GmbH, Seelbach, Germany) was used for all batch equilibrium studies. The X-ray powder diffraction (XRD) patterns were performed via a D8 ADVANCE diffractometer (Bruker AXS Inc, Madison, WI, USA) with a Cu-Kα radiation source (λ = 0.1542 nm) operating at 40 kV, 40 mA, and a scanning range of 2θ = 10–80° at room temperature. The Brunauer–Emmett–Teller (BET) surface area of the synthesized materials was measured using nitrogen sorption isotherms at −195 °C on a model Gemini VII, ASAP 2020 (Micromeritics Instrument, Norcross, GA, USA). Before the analysis, the sample was degassed for 12 h at 110 °C. Zeta potential (ζ) measurements were studied using a Zeta-sizer (Nano ZS, Malvern, UK) for isoelectric point (pH$_{IEP}$) measurements. A JSM-7100F (JEOL) was used to conduct field emission scanning electron microscopy (FE-SEM) measurements.

2.3. Synthesis of Cerium Oxides Nanoparticles

2.3.1. Wet Chemical Precipitation Method

CeO$_2$ NPs were prepared by a wet chemical method via the precipitation of cerium nitrate in an alkaline medium. In a typical procedure, 2 g of Ce(NO$_3$)$_3$·6H$_2$O were dissolved in a mixture of Milli-Q water and ethanol absolute with a ratio of (1:4 *v/v*). Then, this solution was added drop-wise to a freshly prepared 0.4 M sodium hydroxide solution (pH~13) under continuous stirring, and the pH value was controlled at about 11. The mixture was stirred until a yellow suspension of CeO$_2$ NPs was formed after approximately 30 min. After that, the formed precipitate was washed several times with de-ionized water and ethanol absolute so that the soluble salts and fine impurities could be removed. Subsequently, the washed precipitate was centrifuged at 4000 rpm for 15 min and dried in a drying oven at about 50–70 °C for 12 h. The resulting sample is denoted as CP (Chemical Precipitation).

2.3.2. Hydrothermal Modification Method

Hydrothermally modified CeO$_2$ NPs were synthesized according to the same procedure as described in Section 2.3.1 with some modifications using a mixture of absolute ethanol and Milli-Q water (4:1 *v/v*). First, the formed NPs were transferred into a Teflon-lined stainless steel autoclave. Then, the autoclave was sealed and maintained at 150 °C for 12 h. Subsequently, the formed precipitate was washed several times with de-ionized water and ethanol absolute, centrifuged, and dried at about 70 °C for 12 h. The dried material is called HT (Hydrothermal Treatment).

Furthermore, the synthesized CeO$_2$-CP and CeO$_2$-HT NPs were heated at different temperatures: 200 °C and 400 °C with a heating rate of 10 °C/min for 2 h (Figure 1).

2.4. Batch Distribution Studies

2.4.1. Effect of Solution pH

The influence of medium pH on carrier-added [99]Mo uptake on each sorbent was evaluated at a wide range of pH values. For this purpose, we added 30 mL of molybdate solution (50 mg·L^{-1}) to 300 mg of each sorbent. The uptake behavior was investigated at different pH values, which ranged from 1 to 12. The initial pH of the [99]Mo solution was adjusted by using either HNO$_3$ or NaOH. The mixtures were shaken in a thermostatic shaker at 25 $\pm$ 1 °C for 24 h. After that, the liquid phases were separated, centrifuged, and then 1 mL aliquot was withdrawn for radiometric measurements. In these analyses, we measured the total solutions radioactivity before and after equilibration with an HPGe counter by using an appropriate gamma-ray peak (740 keV). Additionally, both initial and equilibrium pH values were measured. Finally, the uptake percent of each material was calculated as a function of solution pH by using the following equation:

$$\text{Uptake}\% = \frac{A_o - A_e}{A_o} \times 100 \tag{1}$$

where A_o and A_e are the initial and equilibrium of ^{99}Mo radioactivity expressed in counts/min.
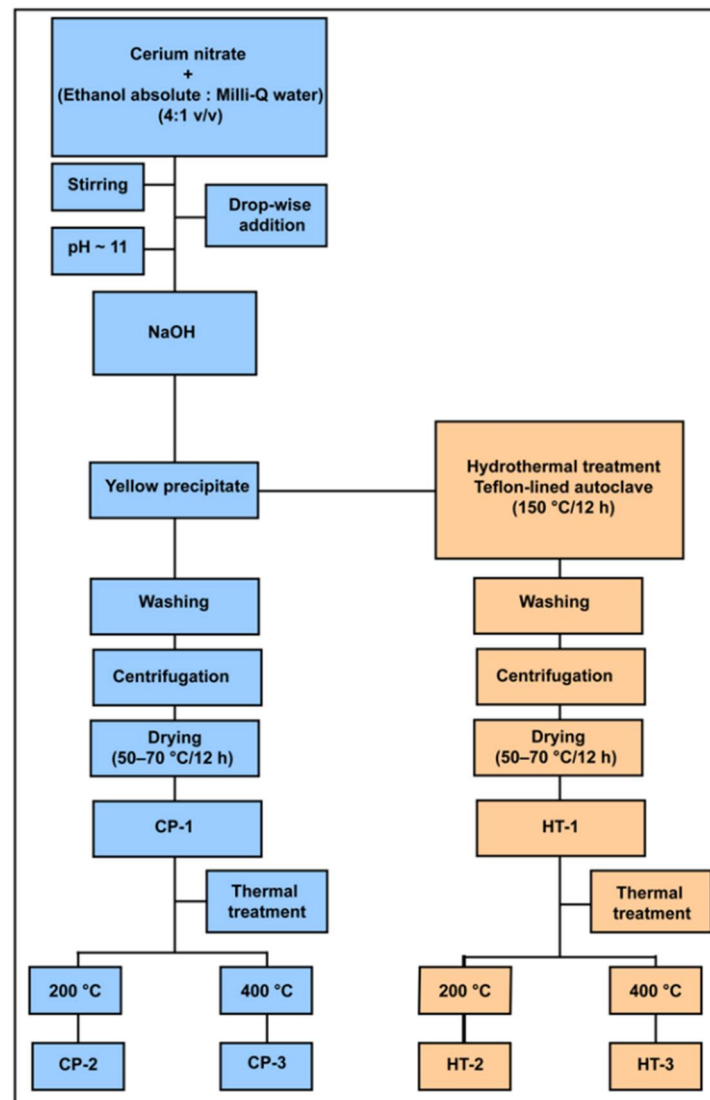

Figure 1. The synthesis protocol of CeO_2 NPs using wet chemical precipitation and hydrothermal modification approaches.

2.4.2. Sorption Kinetics

To estimate the sorption rate of carrier-added ^{99}Mo on the prepared CeO_2 NPs, we determined the uptake percent of ^{99}MoO$_4^{2-}$ ions (~pH 3) at different time intervals. Typically, 300 mg of each sorbent were suspended in 30 mL of ^{99}MoO$_4^{2-}$ solution (50 mg·L^{-1} in 0.001 M HNO$_3$) and shaken in thermostated shaker bath at 25 ± 1 °C for different time intervals (5 min–50 h). Then, 1 mL of the supernatant was separated and measured. The sorption of Mo on each material was followed with time until the equilibrium was established. Finally, we calculated the Mo capacity (Q_t) in mg/g at each time (t) by using the following equation:

$$Q_t = \frac{A_o - A_t}{A_o} \times C_o \times \frac{V}{m} \qquad (2)$$

where A_o (count/min) is the initial activity, and A_t is the ^{99}Mo activity at a time (t), C_o (mg·L^{-1}) is the initial ^{99}MoO$_4^{2-}$ ion concentration, V (L) is the total volume, and m (g) is the sorbent weight.

Furthermore, for a comprehensive understanding of the reaction kinetics and diffusion mechanisms, we used the obtained results and applied different sorption kinetic and diffusion models.

2.4.3. Equilibrium Sorption Isotherms

Sorption isotherm studies were conducted by varying the initial $^{99}MoO_4^{2-}$ ion concentration from 50 to 5000 mg·L^{-1} while keeping the sorbent dose constant. Herein, we mixed 30 mL of ^{99}Mo solution (pH ~ 3) with 300 mg of each material. The other parameters, such as equilibrium time and temperature, were maintained at 24 h and 25 $\pm$ 1 °C, respectively. Subsequently, the aqueous phases were pipetted, centrifuged, and measured. The equilibrium adsorption capacity (Q_e) in mg·g^{-1} was calculated using Equation (2). The obtained results were evaluated using sorption isotherm models.

In order to evaluate sorption isotherm models, three error distribution functions were used. These functions are Chi-square (X^2), average percentage error (APE), and root mean square error (RMSE). These functions can be calculated according to the following equations:

$$X^2 = \sum \frac{\left(Q_{e(exp)} - Q_{e(cal)}\right)^2}{Q_{e(cal)}} \tag{3}$$

$$APE = \left(\sum_1^N \left(\left|Q_{e(exp)} - Q_{e(cal)}\right|/Q_{e(exp)}\right)/N\right) \times 100 \tag{4}$$

$$RMSE = \sqrt{(1/N - 2) \times \sum_1^N \left(Q_{e(exp)} - Q_{e(cal)}\right)^2} \tag{5}$$

2.4.4. Temperature Effects

The change in molybdate uptake was studied under different reaction temperatures. The study was conducted between 298 and 343 K, and the other reaction conditions were kept constant. Moreover, to clarify the thermodynamic nature of the sorption process, we used the obtained data to investigate different thermodynamic parameters. These parameters are the standard enthalpy change ($\Delta H°$), the standard entropy change ($\Delta S°$), and the Gibbs free energy change ($\Delta G°$).

3. Results and Discussion

In order to evaluate the sorption profile of the molybdate on the synthesized CeO_2 NPs, different parameters were studied using the batch contact method. These parameters include solution pH, contact time, initial ion concentration (m_i), and temperature. The impact of each parameter on the Mo sorption was studied separately. Meanwhile, the other factors were kept constant.

3.1. Structural Characterization of the Prepared CeO_2 NPs

The XRD patterns of CeO_2 nanoparticles prepared via wet chemical precipitation and hydrothermal methods are shown in Figure 2. The peaks are indexed using JCPDS card no: 34-0394. All samples of CeO_2 nanoparticles have face centered cubic structure with the lattice parameters a = b = c = 5.411 Å and $\alpha = \beta = \gamma = 90°$. The diffraction peaks were found at 28.56°, 33.08°, 47.47°, 56.36°, 59.08°, 69.40°, and 76.70° [28]. The absence of impurity indicates that both methods synthesize pure CeO_2. The average crystallite size (D) of CeO_2 nanoparticles is calculated by using the Debye–Scherrer equation:

$$D = \frac{K\lambda}{\beta \cos \theta} \tag{6}$$

where λ is the wavelength of the Cu-Kα radiation, K is a constant (=0.89), θ is the diffraction angle, and β is the full width at half maximum (FWHM). The average crystallite size values

for CeO$_2$ nanoparticles were evaluated and listed in Table 1. The results revealed that the thermal treatment affects the crystallite size of the samples prepared by the wet chemical precipitation method. For these samples, elevating the temperature increases the crystallite size. However, in the case of the hydrothermal method, the thermal treatment does not influence the crystallite size.
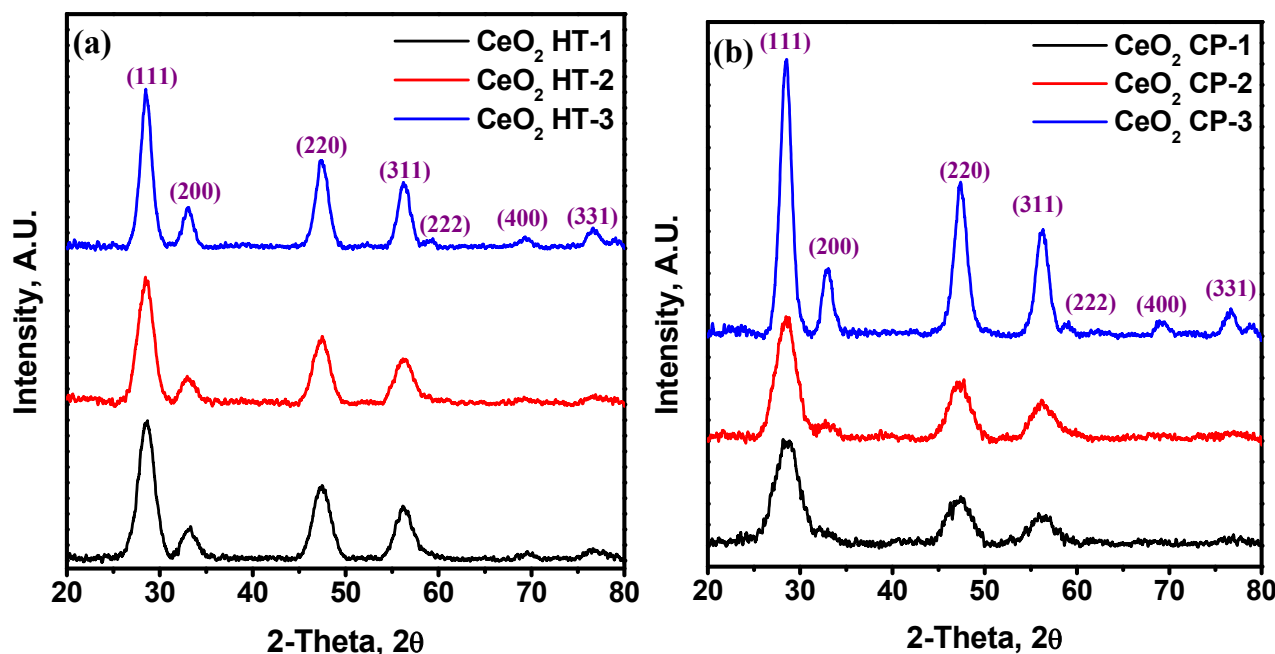

Figure 2. XRD patterns of CeO$_2$ NPs at different temperatures prepared via (**a**) wet chemical precipitation method; (**b**) hydrothermal modification.

Table 1. BET surface area (S$_{BET}$), average pore volume and diameter, crystallite size, and isoelectric point (pH$_{IEP}$) for CeO$_2$ NPs prepared at different conditions.

Sample	S$_{BET}$, (m^2·g^{-1})	Pore Volume, (cm^3·g^{-1})	Pore Size, (nm)	Crystallite Size, (nm)	pH$_{IEP}$
CP-1	150.2	0.085	2.26	2.50	6.91
CP-2	175.3	0.057	2.38	4.62	6.92
CP-3	97.4	0.031	2.33	5.66	6.94
HT-1	187.2	0.128	2.75	3.54	6.99
HT-2	179.8	0.122	2.71	3.61	7.00
HT-3	114.7	0.078	2.71	3.50	7.02

We further examined the textural properties of the CeO$_2$ nanoparticles using a nitrogen adsorption isotherm (Figure 3). All the samples exhibited Type IV isotherms with well-defined H$_2$-type hysteresis loops, which indicates the mesoporous nature of the materials [29]. The BET surface area, pore volume, and pore size of all samples are tabulated in Table 1. The highest BET surface area of the mesoporous CeO$_2$ is 187.2 m^2·g^{-1}. The surface area of the wet chemical precipitation method was increased upon increasing the temperature up to 200 °C and reached 175.3 m^2·g^{-1}, and further thermal treatment resulted in its reduction to 97.4 m^2·g^{-1}. Compared to CeO$_2$ NPs prepared with the wet chemical precipitation method, the hydrothermally modified samples exhibit a higher surface area due to improved surface modification.
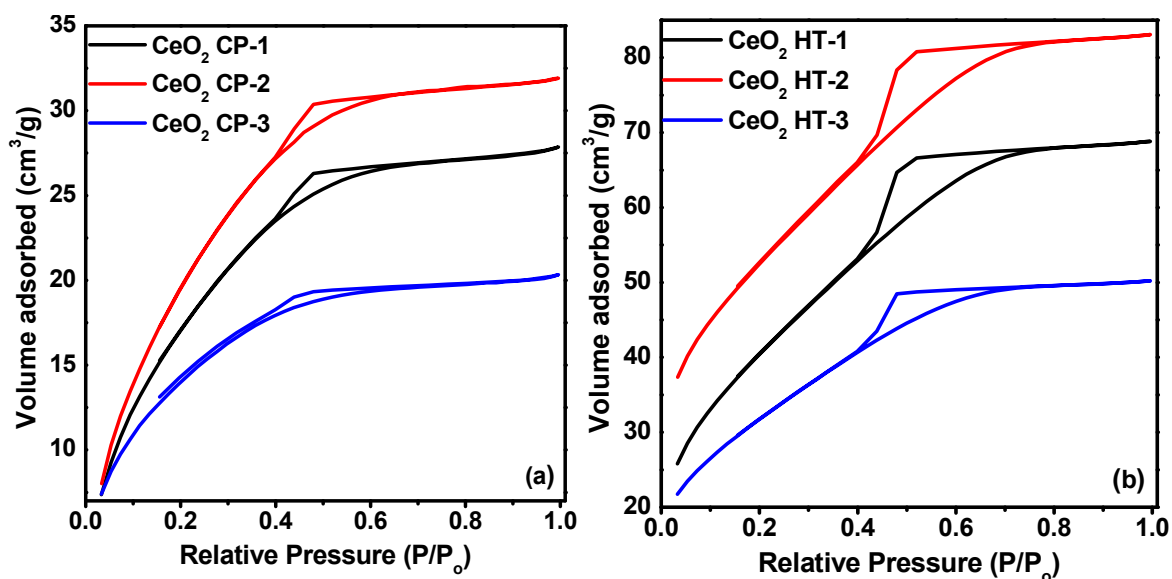
Figure 3. N_2 adsorption–desorption isotherms of CeO_2 NPs at different temperatures prepared via (**a**) wet chemical precipitation method; (**b**) hydrothermal modification.

The zeta potential (ζ) measurements listed in Table 1 give insight into the surface charge. It revealed that the pH_{IEP} of CeO_2 NPs is at about seven. Therefore, the surface of CeO_2 NPs bears a positive charge below pH ~ 7 and a negative charge above this pH value.

Additionally, as the morphology of the nanoparticles is a key characteristic factor for their performance, we investigated the effect of the preparation method with different temperatures on the CeO_2 NPs morphology. Figure 4 presents typical FE-SEM images of CeO_2 NPs prepared at different temperatures. As shown in the SEM images, the hydrothermally prepared CeO_2 NPs exhibited spherical morphology with almost uniform characteristics. There is no obvious change in the morphology upon changing the temperature from 50 °C to 400 °C. The CeO_2 NPs prepared by the wet chemical precipitation method showed a rough morphology compared with the hydrothermally modified analogous especially at a low temperature (50 °C). Upon increasing the temperature, the rough shape was regulated and semi-spherical NPs appeared as shown for CP-2 and CP-3.
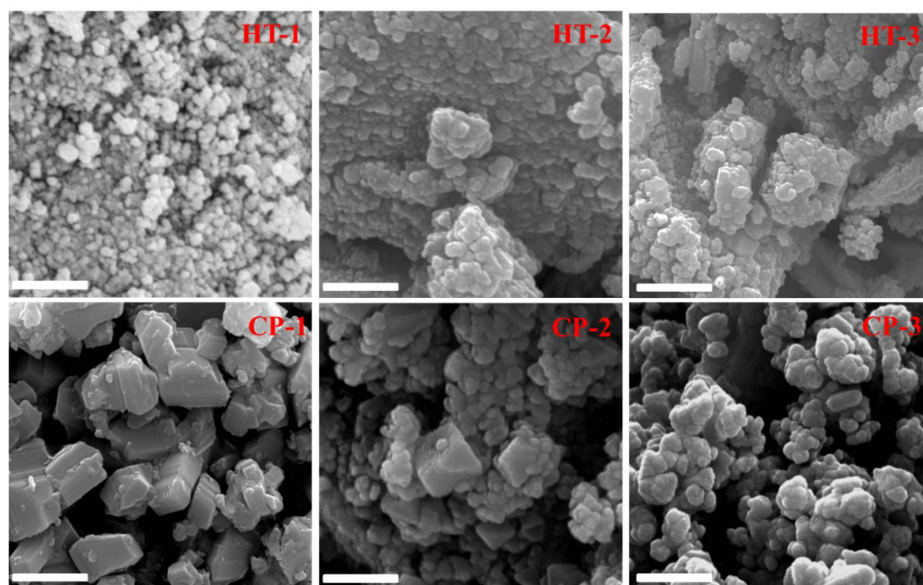

Figure 4. FE-SEM images of CeO_2 NPs at different temperatures prepared via hydrothermal modification (HT) and wet chemical precipitation method (CP).

3.2. Effect of Solution pH

Batch experiments were conducted to verify the usefulness of the synthesized CeO_2 NPs for carrier-added ^{99}Mo sorption from aqueous solutions. The pH of the Mo solution is the key factor that controls the sorption process, as it has a profound impact on determining the ionic state of the functional groups that exist on the sorbent surface. Furthermore, it affects the dissociation, complexation, and/or ionization of the adsorbed ions [30]. In order to predict the optimal experimental conditions for carrier-added ^{99}Mo uptake, the sorption behavior of each material was evaluated at a wide range of pH values (1–12). The results are displayed in Figure 5a. The figure shows that the highest uptake values occur in an acidic medium (pH 2–4). After that, the uptake percent starts to decrease. This behavior can be explained based on two factors: the surface charge of the solid phase and the distribution of the molybdate species in the solution.
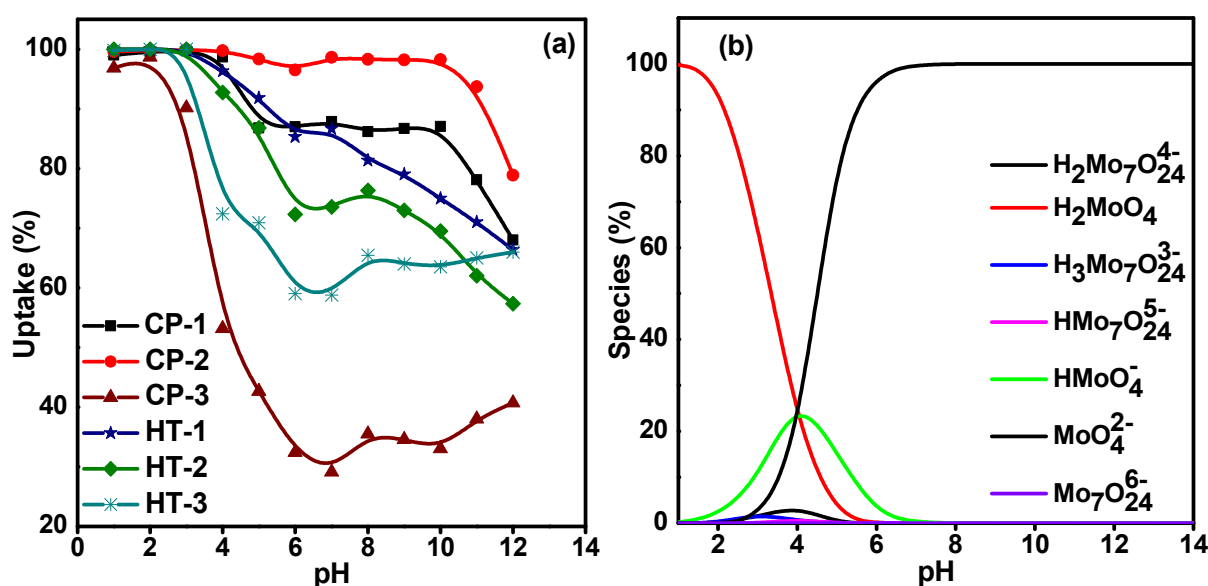

Figure 5. Effect of solution pH on (**a**) the Mo uptake on synthesized CeO_2 NPs ($C_o = 50$ mg·L^{-1}, V/m = 100 mL·g^{-1}, and temperature = 25 ± 1 °C); (**b**) speciation of molybdenum.

Since the external solution pH governs the sorbents' surface acid-base properties, we attempted to clarify the isoelectric point (ζ) of each material. Table 1 shows that the pH_{IEP} is reached at ~pH 7. Consequently, the CeO_2 surface carries a positive charge at low pH (pH < 7). The change in the surface charge of the solid phase is because the active sites on the surface are hydrated and covered by amphoteric hydroxyl groups. Hence, based on the pH of the medium, these hydroxyl groups can undergo different reactions with either H$^+$ or OH$^-$ to develop positive or negative charges on the surface. Herein, at pH < 7, they are protonated, and the CeO_2 surface develops a positive charge as follows:

$$Surface - OH_{Surface} + H^+_{solution} \rightleftharpoons Surface - OH_2^+ \tag{7}$$
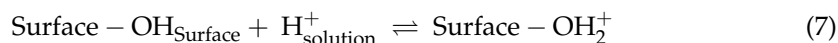
Furthermore, the data in Figure 5a can be interpreted by considering the speciation diagram of molybdenum shown in Figure 5b. The data were calculated with the help of the PHREEQC software (version 3). Molybdenum exists in the solution as molybdate (MoO_4^{2-}). It polymerizes in an acidic medium to polymolybdate ($Mo_7O_{24}^{6-}$) with higher molybdenum content per unit charge [31]. Therefore, an electrostatic attraction between negatively charged molybdate anions and positively charged surfaces occurs.

3.3. Effect of Contact Time

The progress of Mo sorption onto the synthesized CeO_2 was studied at different time intervals, and the results are represented in Figure S1. The data illustrate that for all

sorbents, the uptake percent (U%) of Mo increases with increasing the contact time until a sort of equilibrium state is reached, after which negligible or no further uptake takes place. In more detail, the sorption process took place in two distinct steps. The first one involves a fast uptake rate, which may be attributed to the high availability of active sites on the sorbent surface at the beginning of the sorption reaction. The second one exhibits a relatively slow sorption rate until the equilibrium is established. That is because the number of active sites is rapidly diminished, and the ions have to compete for the sorption sites [32]. Accordingly, under our experimental conditions, the optimum contact times for CP-1, CP-2, CP-3, HT-1, HT-2, and HT-3 are 6 h, 1 h, 30 h, 15 min, 1 h, and 10 h, respectively.

Furthermore, the results revealed that compared to materials prepared via the wet chemical method, the hydrothermally modified samples introduce a faster reaction rate. However, heated materials at 400 °C (CP-3 and HT-3) exhibit a relatively slow sorption rate. This behavior may be explained because the thermal treatment of nanomaterials decreases the number of active surface sites, which reduces the sorbent reactivity [32].

Based on the earlier experimental and surface morphological evaluations, the hydrothermal modification improved the sorption profile of HT-1 considerably. Moreover, except for CP-2, the thermal treatment does not enhance the uptake capability of the heated materials. On the contrary, it adversely diminishes the sorption rate for the ones heated at 400 °C. Therefore, CP-2 and HT-1 were selected for subsequent evaluation studies.

3.3.1. Kinetic Studies

To design an effective sorption process, determining kinetic parameters is crucial [33]. Kinetic modeling provides helpful information about the rate of the sorption process. Therefore, we analyzed the sorption kinetic data of carrier-added ^{99}Mo onto CP-2 and HT-1 by using three different kinetic models, namely, Lagergren-first-order (Equation (8)) [34], pseudo-second-order (Equation (9)) [35], and Elovich (Equation (10)) [36,37]. These models are presented in a non-linear regression form by using the equations as follows:

$$Q_t = Q_e \left(1 - \exp^{-K_1 t}\right) \tag{8}$$

$$Q_t = \frac{K_2 Q_e^2 t}{1 + K_2 Q_e t} \tag{9}$$

$$Q_t = \frac{1}{\beta} \ln(1 + \alpha\beta t) \tag{10}$$

where Q_t and Q_e (mg·g^{-1}) are the amount of adsorbed molybdenum at a time (t) and equilibrium, respectively, k_1 (min^{-1}) is the Lagergren-rate constant, k_2 (g/mg·min) is the pseudo-second-order rate constant, α (mg/g·min) is the Elovich rate constant, and β (mg·g^{-1}) is the desorption constant representing the degree of surface coverage.

Figure 6 displays non-linear fits of sorption kinetic data of Mo onto CP-2 and HT-1 according to the three aforementioned kinetic models by plotting calculated (q_t) values versus contact time (t). The calculated kinetic parameters are presented in Table 2. Good non-linear plots are shown in Figure 6 for all kinetic models under our experimental conditions. Furthermore, by comparing the correlation coefficient values (R^2) of the three applied models (Table 2), it can be seen that the three applied models have close R^2 values. Nonetheless, we can notice that the Elovich model exhibits higher values ($R^2 = 0.999$) than Lagergren-first-order model ($R^2 = 0.989$ and 0.990) and the pseudo-second-order model ($R^2 = 0.991$ and 0.990) for CP-2 and HT-1, respectively. Accordingly, we suggest that the Elovich model is the most appropriate to explain our sorption kinetics data. This finding may indicate that the prepared CeO_2 matrices possess heterogeneous surfaces, and the uptake of carrier-added ^{99}Mo develops multi-adsorption layers [36,37].
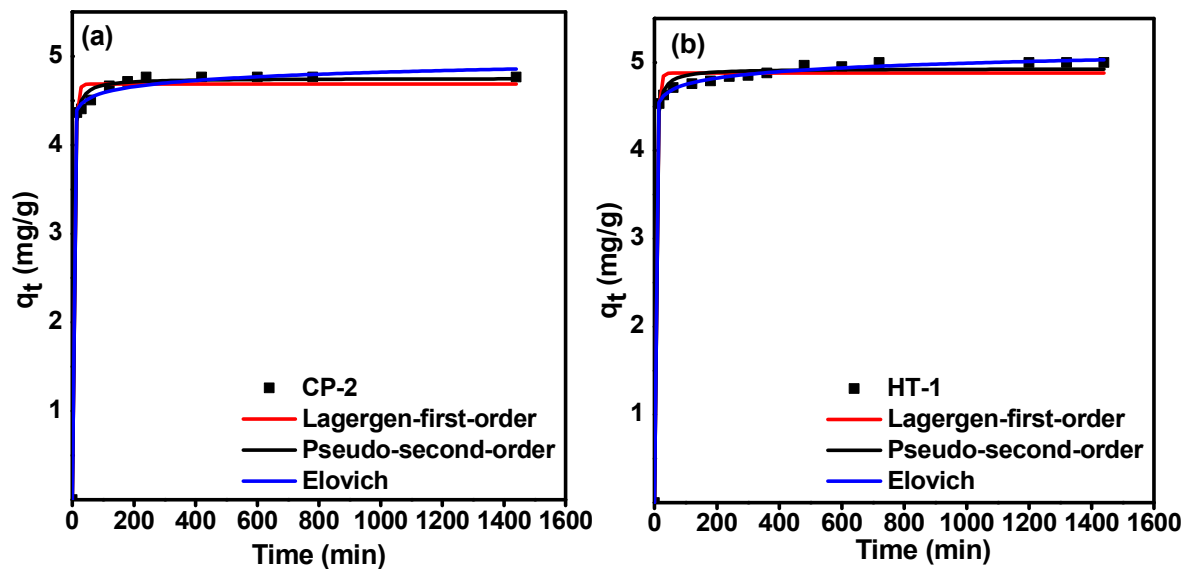
Figure 6. Non-linear fitting of kinetics models (Lagergren-first-order, pseudo-second-order, and Elovich) for the sorption of ^{99}Mo on (**a**) CP-2; (**b**) HT-1.

Table 2. Kinetic parameters for the sorption of carrier-added ^{99}Mo on CP-2 and HT-1.

Kinetic Model	Parameter	CP-2	HT-1
Lageregen-first-order	$q_{e,1}$ (mg·g^{-1})	4.686	4.881
	K_1 (min^{-1})	0.171	0.170
	R^2	0.990	0.989
Pseudo-second-order	$q_{e,2}$ (mg·g^{-1})	4.751	4.930
	K_2 (g/mg·min)	0.128	0.127
	R^2	0.991	0.990
Elovich	α (mg/g·min)	4.724×10^{16}	3.877×10^{16}
	β (g·mg^{-1})	9.874	9.48458
	R^2	0.999	0.999

3.3.2. Diffusion Studies

Generally, the uptake of adsorbate ions on the sorbent material occurs through [38]: (i) the movement of adsorbate ions from the bulk solution to the sorbent surface (bulk diffusion), (ii) the diffusion of adsorbate ions through the liquid film covering the sorbent surface (film diffusion), (iii) internal diffusion of adsorbate ions within the interior pores of the sorbent material (pore diffusion), and (iv) the binding of adsorbate ions on available active sites. In order to investigate the rate-limiting step, three diffusion models are applied. These models are film diffusion (McKay, Equation (11)) [39], intra-particle diffusion (Weber and Morris, Equation (12)) [40], and pore diffusion model (Bangham, Equation (13)) [40]. The models are expressed by the following equations:

$$\ln\left(\frac{1 - Q_t}{Q_e}\right) = -\,k_f t \tag{11}$$

$$Q_t = K_{ip}t^{\frac{1}{2}} + C \tag{12}$$

$$\log\left(\log\left(\frac{C_i}{C_i - Q_t w}\right)\right) = \log\left(\frac{K_b W}{2.303\,V}\right) + \sigma\,\log\,t \tag{13}$$

where Q_t and Q_e (mg·g^{-1}) are the amount of adsorbed molybdenum at a time (t) and equilibrium, respectively. C_i (mg·L^{-1}) is the initial Mo concentration, W (g) is the sorbent mass, and V (L) is the solution volume. k_f (min^{-1}), k_{ip} (mg/g·min$^{1/2}$), and σ are film diffusion, intra-particle diffusion, and pore diffusion rate constants, respectively.

The rate constants can be determined from the slope of the linear plots of $\ln\left(\frac{1-q_t}{q_e}\right)$ versus t (Equation (11)), q_t versus t (Equation (12)), and $\log\left(\log\left(\frac{C_i}{C_i - Q_t w}\right)\right)$ versus t (Equation (13)). The results are shown in Figure 7. The calculated diffusion parameters and the correlation coefficient values (R^2) are tabulated in Table 3. In order to estimate the best mechanism that describes our diffusion data, we compare the correlation coefficient values (R^2) of each model. For CP-2, the application of the McKay model resulted in a higher value ($R^2 = 0.992$) than both Weber and Morris model ($R^2 = 0.977$) and the Bangham model ($R^2 = 0.967$). These findings indicate that the sorption of Mo on CP-2 might occur through an external film diffusion mechanism. For HT-1, the correlation coefficient values of the three models were: McKay model ($R^2 = 0.968$), Weber and Morris model ($R^2 = 0.946$), and Bangham model ($R^2 = 0.980$). Therefore, it can be concluded that the pore diffusion model might control Mo sorption on HT-1.
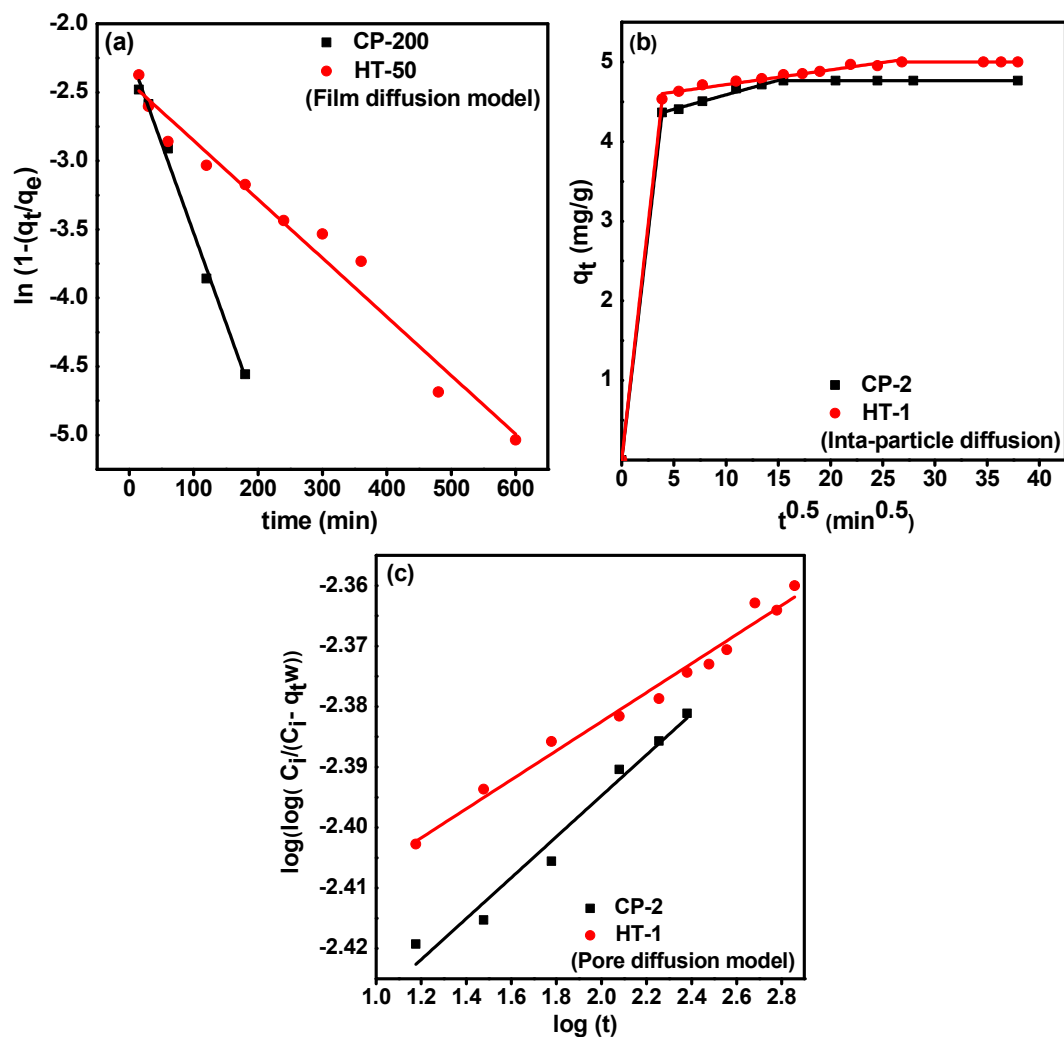

Figure 7. Diffusion plots of (**a**) McKay; (**b**) Weber and Morris; (**c**) Bangham for the sorption of carrier-added [99]Mo on CP-2 and HT-1.

Table 3. Diffusion parameters for the sorption of carrier-added ^{99}Mo on CP-2 and HT-1.

Diffusion Model	Parameter	CP-2	HT-1
McKay (Film diffusion)	k_f (min^{-1})	0.013	0.004
	intercept	-2.218	-2.425
	R^2	0.992	0.968
Weber and Morris (Intra-particle diffusion)	k_{ip} (mg/g·min$^{1/2}$)	0.036	0.019
	Intercept (C) *	4.224	4.531
	R^2	0.977	0.946
Bangham (Pore diffusion)	σ **	0.034	0.024
	intercept	-2.462	-2.431
	R^2	0.967	0.980

* The intercept is influenced by the boundary layer thickness. ** σ value should be <1.

3.4. Equilibrium Isotherm Studies

Sorption isotherms describe how the adsorbed ions are dispersed between liquid and solid phases when the adsorption process reaches an equilibrium state at a constant temperature [41,42]. Consequently, a proper interpretation of equilibrium isotherms is necessary to improve the sorption mechanism and design an effective sorption system [31,43,44]. Figure 8 illustrates the influence of initial molybdate concentration on the equilibrium sorption capacity (Q_e) and the uptake percent of Mo onto CP-2 and HT-1 at constant temperature (25 ± 1 °C). The figure shows that on increasing the initial Mo concentration, the uptake percent decreases, and on the contrary, the sorption capacity (Q_e) increases. These findings are attributed to the increased mass driving force at higher molybdate concentrations [45–47].
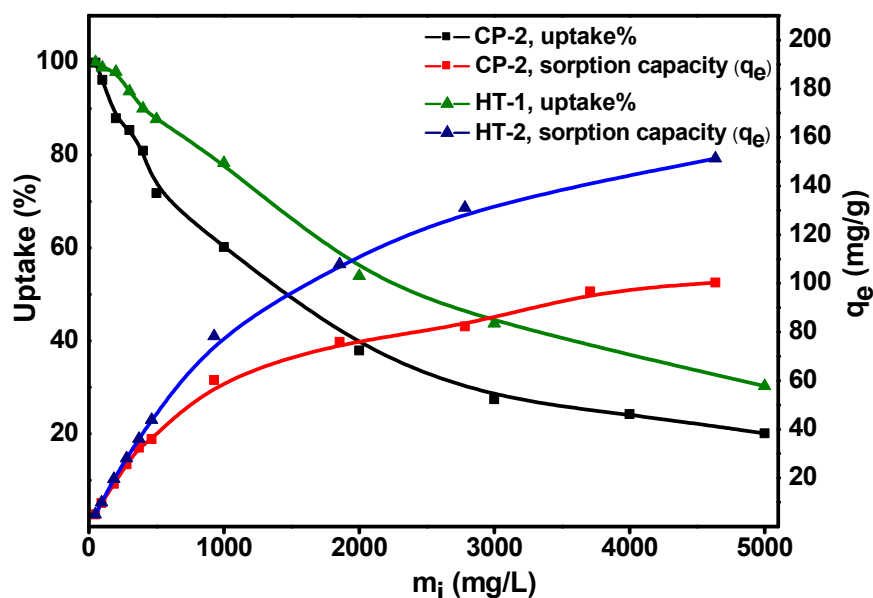

Figure 8. Effect of initial molybdate concentration on the uptake percent and equilibrium sorption capacity (Q_e) of carrier-added ^{99}Mo on CP-2 and HT-1 (pH = 3, V/m = 100 mL·g^{-1}, t = 24 h, and temperature = 25 ± 1 °C).

Based on the sorbents' behavior and the mode of interaction, the equilibrium isotherm data shown in Figure 8 were modeled. We applied three widely-used two-parameters, and

isotherm models. These models are Freundlich [48], Langmuir [49], and Temkin [50]. The non-linear regressions of these models are represented by Equations (14)–(16), respectively:

$$Q_e = K_F C_e^{\frac{1}{n}} \tag{14}$$

$$Q_e = \frac{Q_m K_l C_e}{1 + (K_l C_e)} \tag{15}$$

$$Q_e = \frac{RT}{b_t} \ln(A_t C_e) \tag{16}$$

where Q_e (mg·g^{-1}) is the equilibrium sorption capacity, C_e (mg·L^{-1}) is the equilibrium concentration of molybdate ions, Q_m (mg·g^{-1}) is the maximum capacity. K_F (mg^{1-n}·L^n/g), K_L (L·mg^{-1}), and A_t (L·g^{-1}) are the Freundlich, Langmuir, and Temkin constants, respectively. The parameters *n* and *B* reflect the heterogeneity of adsorption sites and the heat of adsorption, respectively. R is the universal gas constant (0.008314 kJ·mol^{-1}·K^{-1}), and T (K) is the absolute temperature.

Figure 9 introduces the non-linear fits of isotherm data of Mo onto CP-2 and HT-1 for the three isotherms models mentioned above by plotting calculated (Q_e) values versus (C_e). The calculated equilibrium isotherm parameters and their corresponding correlation coefficient (R^2) are given in Table 4. According to the correlation coefficient (R^2) values, the Freundlich isotherm best describes the equilibrium data. It has a higher correlation coefficient (R^2 = 0.986, 0.989) than Langmuir (R^2 = 0.958, 0.983) and Temkin (R^2 = 0.794, 0.756) for CP-2 and HT-1, respectively. This result is confirmed by the lower values of the error functions (X^2), (APE), and (RMSE) for the Freundlich isotherm compared to the Langmuir and Temkin models (Table 4). Furthermore, the sorption intensity (n) values (for the Freundlich isotherm) are 3.35 (for CP-2) and 3.98 (for HT-1), which indicates a favorable sorption process. This result shows that CP-2 and HT-1 have heterogeneous surfaces with a wide distribution of non-equivalent sorption sites.
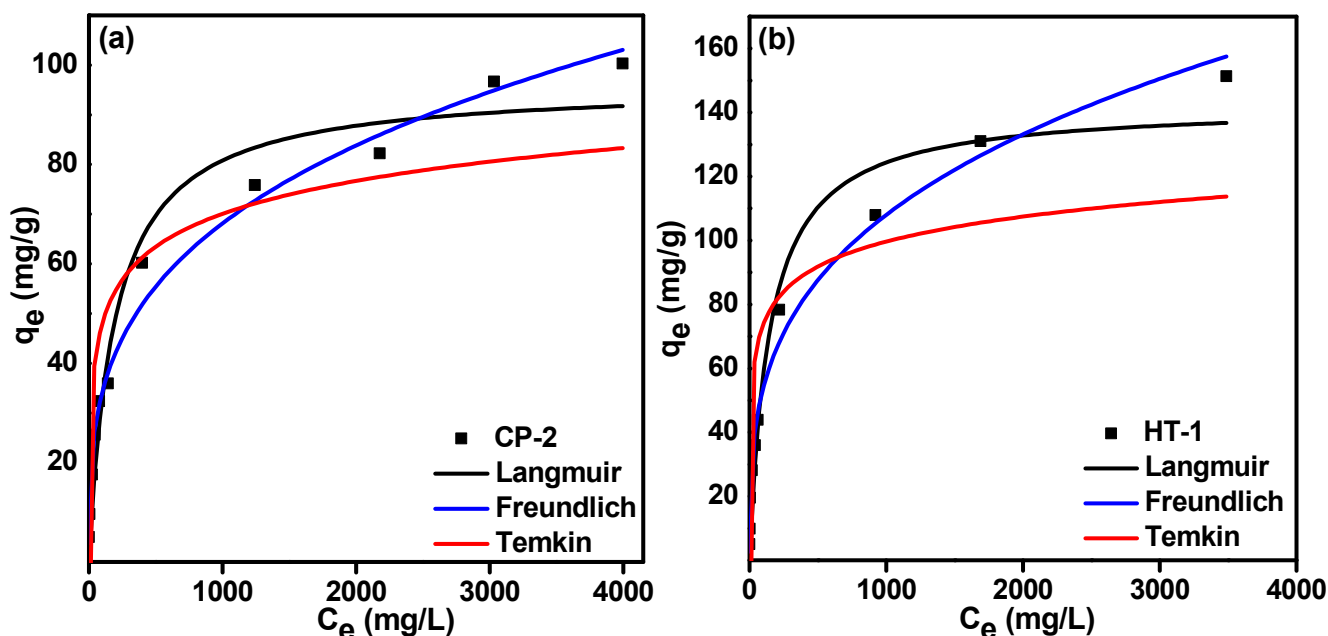

Figure 9. Equilibrium isotherms (Langmuir, Freundlich, and Temkin) of carrier-added ^{99}Mo on (**a**) CP-2; (**b**) HT-1.

Table 4. Isotherm parameters and error functions calculations for the sorption of carrier-added ^{99}Mo on CP-2 and HT-1.

Isotherm Model	Parameter	CP-2	HT-1
Langmuir	Q_{max} (mg·g^{-1})	96.083	109.114
	K_L (L·mg^{-1})	0.005	0.012
	R^2	0.958	0.983
	X^2	41.989	138.843
	APE	28.75	36.032
	RMSE	7.190	11.185
Freundlich	K_F (mg^{1-n}·L^n·g^{-1})	8.668	15.078
	n	3.350	3.981
	R^2	0.986	0.989
	X^2	3.888	4.678
	APE	11.442	15.304
	RMSE	4.060	5.524
Temkin	b_t	0.260	0.266
	A_t (L·g^{-1}) *	1.535	8.199
	R^2	0.794	0.756
	X^2	32.407	70.355
	APE	81.781	137.723
	RMSE	15.917	28.175

* A_t is the equilibrium-binding constant that corresponds to the maximum binding energy.

Furthermore, the maximum sorption capacity for Mo was evaluated under static conditions. We conducted repeated equilibrations of carrier-added ^{99}Mo with CP-2 and HT-1 at 25 ± 1 °C until no further uptake occurred. The maximum sorption capacity was determined according to the following equation:

$$Q_{max} = \frac{\sum Uptake\%}{100} \times C_o \times \frac{V}{m} \qquad (17)$$

where Q_{max} (mg·g^{-1}) is the maximum (saturation) sorption capacity, C_o (mg·L^{-1}) is the initial concentration, V (L) is the volume of the aqueous phase, and m (g) is the matrix weight.

The results show that the sorption capacities of CP-2 and HT-1 reach 184 ± 12 and 192 ± 10 mg Mo·g^{-1}, respectively. These values might be attributed to the high surface area of CP-2 and HT-1. In addition, the sorption behavior of each sorbent allows the formation of multi-adsorption layers on their surfaces, which is confirmed by kinetic and equilibrium isotherm studies. It is pertinent to point out that the sorption capacities of CeO$_2$ nanosorbents we developed are much higher than the sorption capacity of conventional alumina (2–20 mg Mo·g^{-1}) [8]. Therefore, the new materials have the potential to be implemented to produce ^{99}Mo/^{99m}Tc generators by using LSA ^{99}Mo.

3.5. Thermodynamic Studies

The effect of temperature on molybdenum uptake onto CP-2 and HT-1 was studied in the temperature range (298–343 K). With increasing the reaction temperature, a slight increase in carrier-added ^{99}Mo uptake is observed on HT-1. Meanwhile, the sorption capacity of CP-2 increases noticeably. These findings indicate that the sorption process is endothermic in nature.

In order to understand the thermodynamic behavior of the sorption process, we investigated the values of the enthalpy change (ΔH°), the entropy change (ΔS°), and the free energy change (ΔG°) in our experimental temperature window. These parameters were calculated by using Vant' Hoff equations [51], as follows:

$$\ln K_d = \left(-\frac{\Delta H^\circ}{RT}\right) + \left(\frac{\Delta S^\circ}{R}\right) \qquad (18)$$

$$\Delta G^\circ = \Delta H^\circ - T\Delta S^\circ \qquad (19)$$

$$\Delta G^\circ = -RT\ln K_d \qquad (20)$$

where K_d ($mg\cdot mL^{-1}$) is the distribution coefficient, R is the universal gas constant ($0.008314\ kJ\cdot mol^{-1}\cdot K^{-1}$), and T (K) is the absolute temperature.

Figure 10 shows linear plots of $\ln K_d$ versus the reciprocal absolute temperature (1/T). The values of ΔH° and ΔS° can be determined from the slope and intercept, respectively. The calculated values of ΔH°, ΔS°, and ΔG° are listed in Table 5. The positive values of ΔH° indicate that the sorption processes of Mo onto CP-2 and HT-1 are endothermic. In addition, the positive values of ΔS° point to the increase in randomness at the solid–liquid interface. Moreover, the negative values of ΔG° confirm the spontaneous nature of the sorption processes under our experimental conditions [52].
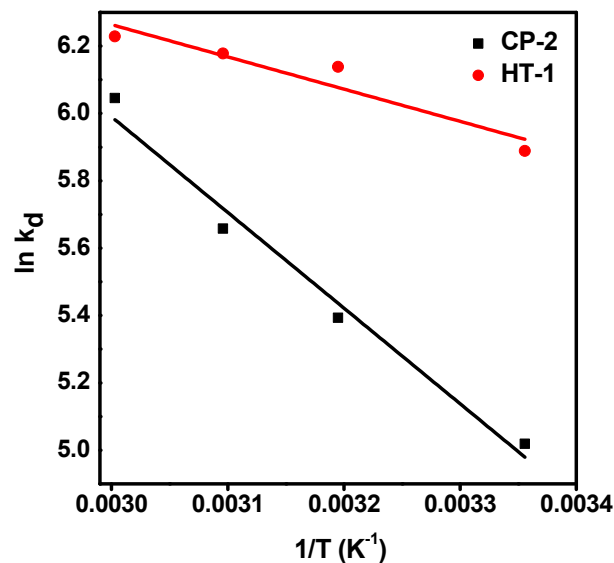

Figure 10. Van't Hoff plot for the sorption of carrier-added [99]Mo on CP-2 and HT-1 ($C_o = 1000\ mg\cdot L^{-1}$, pH = 3, V/m = 100 $mL\cdot g^{-1}$, and t = 24 h).

Table 5. Thermodynamic parameters for the sorption of carrier-added [99]Mo on CP-2 and HT-1.

CeO$_2$ NPs	Temperature (K)	ΔG° (kJ·mol^{-1})	ΔH° (kJ·mol^{-1})	ΔS° (kJ·mol^{-1}·K^{-1})	R^2
CP-2	298	−12.338	23.620	0.121	0.970
	313	−14.149			
	323	−15.355			
	333	−16.562			
HT-1	298	−14.676	7.959	0.076	0.867
	313	−15.816			
	323	−16.575			
	333	−17.335			

4. Summary and Conclusions

Our main goal was to evaluate the sorption profile of LSA ^{99}Mo on several CeO$_2$ nanosorbents developed in our laboratory. First, these materials were synthesized by using simple wet-chemical precipitation (CP) and hydrothermal (HT) methods. Then, they were heated at different temperatures: 200 °C and 400 °C. Eventually, an assessment of the carrier-added ^{99}Mo uptake behavior was carried out under different experimental conditions. We found that the hydrothermal modification improves the morphological and sorption profile of HT-1 considerably. Except for CP-2, the thermal treatment did not enhance the sorption capability of the heated materials. In contrast, it diminished the Mo sorption for the ones heated at 400 °C. In addition, sorption kinetics data of carrier-added ^{99}Mo Mo onto CP-2 and HT-1 were most favorably described by the Elovich model. The diffusion data showed that film and pore diffusion models controlled the sorption process for CP-2 and HT-1, respectively. Moreover, out of the investigated isotherm models, the Freundlich model was the most appropriate to describe the equilibrium isotherms of carrier-added ^{99}Mo on both sorbents. Furthermore, we studied the influence of reaction temperature on Mo uptake, and the results confirmed the spontaneous and endothermic nature of the sorption processes. Finally, we evaluated the maximum sorption capacity of CP-2 and HT-1 towards carrier-added ^{99}Mo under static sorption conditions. Their capacity reached 184 ± 12 and 192 ± 10 mg Mo.g^{-1}, respectively. From the outcome of our investigation, it is possible to conclude that HT-1 and CP-2 have favorable sorption profiles and appreciable uptake capacities for carrier-added ^{99}Mo. Consequently, they have the potential for producing a ^{99m}Tc radionuclide generator by using LSA ^{99}Mo. Clearly, the next stage of our research will investigate the feasibility of using these two sorbent materials to develop a useful ^{99}Mo/^{99m}Tc generator.

Author Contributions: M.F.N.; Suggested the research idea, conducted the experiments, analyzed the data, drafted the original manuscript, and acquisition of the financial support for the project leading to this publication. A.F.E.-D. and M.M.; carried out the characterization measurements, co-analyzed the data, and reviewed the original draft. A.T.; supervised the project and reviewed the original draft. All authors have read and agreed to the published version of the manuscript.

Institutional Review Board Statement: Not applicable.

Informed Consent Statement: Not applicable.

Data Availability Statement: Data is contained within the article.

Conflicts of Interest: The authors declare no conflict of interest.

References

1. Ruan, Q.; Gan, Q.; Zhang, X.; Fang, S.; Zhang, J. Preparation and Bioevaluation of Novel ^{99m}Tc-Labeled Complexes with a 2-Nitroimidazole HYNIC Derivative for Imaging Tumor Hypoxia. *Pharmaceuticals* **2021**, *14*, 158. [CrossRef] [PubMed]
2. Gumiela, M. Cyclotron production of ^{99m}Tc: Comparison of known separation technologies for isolation of ^{99m}Tc from molybdenum targets. *Nucl. Med. Biol.* **2018**, *58*, 33–41. [CrossRef]

3. Martini, P.; Boschi, A.; Cicoria, G.; Zagni, F.; Corazza, A.; Uccelli, L.; Pasquali, M.; Pupillo, G.; Marengo, M.; Loriggiola, M.; et al. In-house cyclotron production of high-purity Tc-99m and Tc-99m radiopharmaceuticals. *Appl. Radiat. Isot.* **2018**, *139*, 325–331. [CrossRef] [PubMed]
4. Urbano, N.; Scimeca, M.; Tancredi, V.; Bonanno, E.; Schillaci, O. ^{99m}Tc-sestamibi breast imaging: Current status, new ideas and future perspectives. *Semin. Cancer Biol.* **2020**, in press. [CrossRef] [PubMed]
5. Chakravarty, R.; Dash, A.; Venkatesh, M. A novel electrochemical technique for the production of clinical grade ^{99m}Tc using $(n,\gamma)^{99}$Mo. *Nucl. Med. Biol.* **2010**, *37*, 21–28. [CrossRef] [PubMed]
6. Chang, S.H. Types of bulk liquid membrane and its membrane resistance in heavy metal removal and recovery from wastewater. *Desalin. Water Treat.* **2016**, *57*, 19785–19793. [CrossRef]
7. I.A.E.A. *Radiotracer Generators for Industrial Applications*; International Atomic Energy Agency: Vienna, Austria, 2013.
8. Molinski, V.J. A review of ^{99m}Tc generator technology. *Int. J. Appl. Rad. Isot.* **1982**, *33*, 811–819. [CrossRef]
9. I.A.E.A. *Cyclotron Based Production of Technetium-99m*; International Atomic Energy Agency: Vienna, Austria, 2017.
10. Nawar, M.F.; Türler, A. Development of New Generation of ^{99}Mo/^{99m}Tc Radioisotope Generators to Meet the Continuing Clinical Demands. In Proceedings of the 2nd International Conference on Radioanalytical and Nuclear Chemistry (RANC 2019), Budapest, Hungary, 5–10 May 2019.
11. Knapp, F., Jr.; Baum, R. Radionuclide generators-a new renaissance in the development of technologies to provide diagnostic and therapeutic radioisotopes for clinical applications. *Curr. Radiopharm.* **2012**, *5*, 175–177. [CrossRef]
12. Osso, J.A., Jr.; Catanoso, M.F.; Barrio, G.; Brambilla, T.P.; Teodoro, R.; Dias, C.R.B.R.; Suzuki, K.N. Technetium-99m: New Production and Processing Strategies to Provide Adequate Levels for SPECT Imaging. *Curr. Radiopharm.* **2012**, *5*, 178–186. [CrossRef]
13. N.A.P. *Molybdenum-99 for Medical Imaging*; The National Academies Press: Washington, DC, USA, 2016. [CrossRef]
14. Qaim, S.M. The present and future of medical radionuclide production. *Radiochim. Acta* **2012**, *100*, 635–651. [CrossRef]
15. I.A.E.A. *Non-HEU Production Technologies for Molybdenum-99 and Technetium-99m*; International Atomic Energy Agency: Vienna, Austria, 2013.
16. I.A.E.A. *Feasibility of Producing Molybdenum-99 on a Small Scale Using Fission of Low Enriched Uranium or Neutron Activation of Natural Molybdenum*; International Atomic Energy Agency: Vienna, Austria, 2015.
17. Evans, J.V.; Moore, P.W.; Shying, M.E.; Sodeau, J.M. Zirconium molybdate gel as a generator for technetium-99m—I. The concept and its evaluation. *Int. J. Rad. Appl. Instrum. A* **1987**, *38*, 19–23. [CrossRef]
18. Maoliang, L. Production of gel-type Tc-99m generator for nuclear medicine. In Proceedings of the 12th KAIF/KNS Annual Conference, Seoul, Korea, 3–4 April 1997.
19. Mostafa, M.; Saber, H.M.; El-Sadek, A.A.; Nassar, M.Y. Preparation and performance of ^{99}Mo/^{99m}Tc chromatographic column generator based on zirconium molybdosilicate. *Radiochim. Acta* **2016**, *104*, 257–265. [CrossRef]
20. Sekimoto, S.; Tatenuma, K.; Suzuki, Y.; Tsuguchi, A.; Tanaka, A.; Tadokoro, T.; Kani, Y.; Morikawa, Y.; Yamamoto, A.; Ohtsuki, T. Separation and purification of ^{99m}Tc from ^{99}Mo produced by electron linear accelerator. *J. Radioanal. Nucl. Chem.* **2017**, *311*, 1361–1366. [CrossRef]
21. Sebastian, V.; Arruebo, M.; Santamaria, J. Reaction Engineering Strategies for the Production of Inorganic Nanomaterials. *Small* **2014**, *10*, 835–853. [CrossRef] [PubMed]
22. Jadhav, A. Wet Chemical Methods for Nanop article Synthesis. In *Chemical Methods for Processing Nanomaterials*, 1st ed.; Singh, V.N., Ed.; CRC Press: Boca Raton, FL, USA, 2021; pp. 49–58.
23. Baig, N.; Kammakakam, I.; Falath, W. Nanomaterials: A review of synthesis methods, properties, recent progress, and challenges. *Mater. Adv.* **2021**, *2*, 1821–1871. [CrossRef]
24. Priya, S.D.; Nesaraj, A.S.; Selvakumar, A.I. Facile wet-chemical synthesis and evaluation of physico-chemical characteristics of novel nanocrystalline NdCoO$_3$-based perovskite oxide as cathode for LT-SOFC applications. *Bull. Mater. Sci.* **2021**, *44*, 115. [CrossRef]
25. Gan, Y.X.; Jayatissa, A.H.; Yu, Z.; Chen, X.; Li, M. Hydrothermal Synthesis of Nanomaterials. *J. Nanomater.* **2020**, *2020*, 8917013. [CrossRef]
26. Kigozi, M.; Ezealigo, B.N.; Onwualu, A.P.; Dzade, N.Y. Hydrothermal Synthesis of Metal Oxide Composite Cathode Materials for High Energy Application. In *Chemically Deposited Nanocrystalline Metal Oxide Thin Films: Synthesis, Characterizations, and Applications*, 1st ed.; Ezema, F.I., Lokhande, C.D., Rajan, J., Eds.; Springer International Publishing: Cham, Switzerland, 2021; pp. 489–508. [CrossRef]
27. Sakr, T.M.; Nawar, M.F.; Fasih, T.; El-Bayoumy, S.; Abd El-Rehim, H.A. Nano-technology contributions towards the development of high performance radioisotope generators: The future promise to meet the continuing clinical demand. *Appl. Radiat. Isot.* **2017**, *129*, 67–75. [CrossRef]
28. Madkour, M.; Allam, O.G.; Abdel Nazeer, A.; Amin, M.O.; Al-Hetlani, E. CeO$_2$-based nanoheterostructures with p–n and n–n heterojunction arrangements for enhancing the solar-driven photodegradation of rhodamine 6G dye. *J. Mater. Sci. Mater. Electron.* **2019**, *30*, 10857–10866. [CrossRef]
29. Zhu, H.; Chen, Y.; Wang, Z.; Liu, W.; Wanga, L. Catalytic oxidation of CO over mesoporous copper-doped ceria catalysts via a facile CTAB-assisted synthesis. *RSC Adv.* **2018**, *8*, 14888–14897. [CrossRef]

30. Ivanets, A.; Kitikova, N.; Shashkova, I.; Radkevich, A.; Stepanchuk, T.; Maslova, M.; Mudruk, N. One-Stage Adsorption Treatment of Liquid Radioactive Wastes with Complex Radionuclide Composition. *Water Air Soil Pollut.* **2020**, *231*, 144. [CrossRef]

31. Metwally, S.S.; Attallah, M.F. Impact of surface modification of chabazite on the sorption of iodine and molybdenum radioisotopes from liquid phase. *J. Mol. Liq.* **2019**, *290*, 111237. [CrossRef]

32. Hashem, A.; Sanousy, M.A.; Mohamed, L.A.; Okoye, P.U.; Hameed, B.H. Natural and Low-Cost P. turgidum for Efficient Adsorption of Hg(II) Ions from Contaminated Solution: Isotherms and Kinetics Studies. *J. Polym. Environ.* **2021**, *29*, 304–312. [CrossRef]

33. Maamoun, I.; Eljamal, R.; Falyouna, O.; Bensaida, K.; Sugihara, Y.; Eljamal, O. Insights into kinetics, isotherms and thermodynamics of phosphorus sorption onto nanoscale zero-valent iron. *J. Mol. Liq.* **2021**, *328*, 115402. [CrossRef]

34. Lagergren, S.K. About the theory of so-called adsorption of soluble substances. *K. Sven. Vetensk. Handl.* **1898**, *24*, 1–39.

35. Jasper, E.E.; Ajibola, V.O.; Onwuka, J.C. Nonlinear regression analysis of the sorption of crystal violet and methylene blue from aqueous solutions onto an agro-waste derived activated carbon. *Appl. Water Sci.* **2020**, *10*, 132. [CrossRef]

36. Hashem, A.; Badawy, S.M.; Farag, S.; Mohamed, L.A.; Fletcher, A.J.; Taha, G.M. Non-linear adsorption characteristics of modified pine wood sawdust optimised for adsorption of Cd(II) from aqueous systems. *J. Environ. Chem. Eng.* **2020**, *8*, 103966. [CrossRef]

37. Chatterjee, R.; Majumder, C. Modelling of adsorption process in industrial wastewater treatment—A review. *J. Indian Chem. Soc.* **2019**, *96*, 499–506. [CrossRef]

38. Pholosi, A.; Naidoo, E.B.; Ofomaja, A.E. Intraparticle diffusion of Cr(VI) through biomass and magnetite coated biomass: A comparative kinetic and diffusion study. *S. Afr. J. Chem. Eng.* **2020**, *32*, 39–55. [CrossRef]

39. McKay, G.; Poots, V.J.P. Kinetics and diffusion processes in colour removal from effluent using wood as an adsorbent. *J. Chem. Technol. Biotechnol.* **1980**, *30*, 279–292. [CrossRef]

40. Weber, W.J.; Morris, J.C. Kinetics of Adsorption on Carbon from Solution. *J. Sanit. Eng. Div.* **1963**, *89*, 31–59. [CrossRef]

41. Hassan, H.S.; Elmaghraby, E.K. Retention behavior of cesium radioisotope on poly (acrylamido-sulfonic acid) synthesized by chain polymerization. *Appl. Radiat. Isot.* **2019**, *146*, 40–47. [CrossRef] [PubMed]

42. Khandaker, S.; Toyohara, Y.; Saha, G.C.; Awual, M.R.; Kuba, T. Development of synthetic zeolites from bio-slag for cesium adsorption: Kinetic, isotherm and thermodynamic studies. *J. Water Process. Eng.* **2020**, *33*, 101055. [CrossRef]

43. Benmessaoud, A.; Nibou, D.; Mekatel, E.H.; Amokrane, S. A Comparative Study of the Linear and Non-Linear Methods for Determination of the Optimum Equilibrium Isotherm for Adsorption of Pb^{2+} Ions onto Algerian Treated Clay. *Iran. J. Chem. Chem. Eng.* **2020**, *39*, 153–171. [CrossRef]

44. Mahmoud, M.E.; Saad, E.A.; El-Khatib, A.M.; Soliman, M.A.; Allam, E.A. Adsorptive removal of radioactive isotopes of cobalt and zinc from water and radioactive wastewater using TiO_2/Ag_2O nanoadsorbents. *Prog. Nucl. Energy* **2018**, *106*, 51–63. [CrossRef]

45. Karimzadeh, L.; Lippold, H.; Stockmann, M.; Fischer, C. Effect of DTPA on europium sorption onto quartz—Batch sorption experiments and surface complexation modeling. *Chemosphere* **2020**, *239*, 124771. [CrossRef]

46. Luo, W.; Chen, J.; Lin, H.; Ye, X. Biomass base membrane with phenol hydroxy-amino group for ultraselective adsorption of radioactive Co(II) in trace concentration. *Sep. Purif. Technol.* **2021**, *272*, 118878. [CrossRef]

47. Awual, M.R.; Khraisheh, M.; Alharthi, N.H.; Luqman, M.; Islam, A.; Karim, M.R.; Rahman, M.M.; Khaleque, M.A. Efficient detection and adsorption of cadmium(II) ions using innovative nano-composite materials. *Chem. Eng. J.* **2018**, *343*, 118–127. [CrossRef]

48. Zsigmondy, R. Über amikroskopische Goldkeime. I. *Z. Für Phys. Chem.* **1906**, *56U*, 65–76. [CrossRef]

49. Langmuir, I. The Adsorption of Gases on Plane Surfaces of Glass, Mica and Platinum. *J. Am. Chem. Soc.* **1918**, *40*, 1361–1403. [CrossRef]

50. Temkin, M.; Pyzhev, V. Recent modifications to Langmuir isotherms. *Acta Physiochim. URSS* **1940**, *12*, 217–225.

51. Chen, T.; Wang, Q.; Lyu, J.; Bai, P.; Guo, X. Boron removal and reclamation by magnetic magnetite (Fe_3O_4) nanoparticle: An adsorption and isotopic separation study. *Sep. Purif. Technol.* **2020**, *231*, 115930. [CrossRef]

52. Marcu, C.; Balla, A.; Balázs, J.Z.S.; Lar, C. Adsorption Isotherms and Thermodynamics for Chromium(VI) Using an Anion Exchange Resin. *Anal. Lett.* **2021**, *54*, 1783–1793. [CrossRef]